# An Immersed Interface Method for Incompressible Flows and Near Contact

Michael J. Facci<sup>1</sup> and Boyce E. Griffith\*1-5

<sup>1</sup>Department of Mathematics, University of North Carolina, Chapel Hill, NC, USA
 <sup>2</sup>Department of Biomedical Engineering, University of North Carolina, Chapel Hill, NC, USA
 <sup>3</sup>Carolina Center for Interdisciplinary Applied Mathematics, University of North Carolina, Chapel Hill, NC, USA
 <sup>4</sup>Computational Medicine Program, University of North Carolina School of Medicine, Chapel Hill, NC, USA
 <sup>5</sup>McAllister Heart Institute, University of North Carolina School of Medicine, Chapel Hill, NC, USA

October 31, 2025

#### **Abstract**

We present an enhanced immersed interface method for simulating incompressible fluid flows in thin gaps between closely spaced immersed boundaries. This regime, common in engineered structures such as including tribological interfaces and bearing assemblies, poses significant computational challenges because of limitations in grid resolution and the prohibitive cost of mesh refinement near contact. The immersed interface method imposes jump conditions that capture stress discontinuities generated by forces that are concentrated along immersed boundaries. Our approach introduces a bilinear velocity interpolation operator that incorporates jump conditions from multiple nearby interfaces when they occupy the same interpolation stencil. Numerical results demonstrate substantial improvements in both interface and Eulerian velocity accuracy compared to lubrication-based immersed boundary and immersed interface methods. The proposed method improves upon previous interpolation schemes, and eliminates the need for prior knowledge of interface orientation or geometry. This makes it broadly applicable to a wide range of fluid–structure interaction problems involving near-contact dynamics.

**Keywords:** immersed interface method, near contact, incompressible flow, fluid–structure interaction, discrete surface, finite element, jump condition

#### 1 Introduction

Simulating the dynamics of interactions between fluid flows and immersed boundaries has a broad range of applications in science and engineering. These include heart valves, <sup>1,2</sup> bio-locomotion for swimmers, <sup>3</sup> inferior vena cava filters, <sup>4</sup> red blood cell aggregation, <sup>5,6</sup> and prosthetic joint lubrication. <sup>7</sup> The immersed boundary (IB) method and its extensions are widely used for such applications. The

<sup>\*</sup>Corresponding author: boyceg@email.unc.edu

immersed interface method (IIM) is a particular approach to such models that enforces the jump conditions associated with interfacial forces concentrated along fluid–structure boundaries.

The IIM originated in work by Mayo<sup>8</sup> and by LeVeque and Li<sup>9</sup> for the solution of elliptic partial differential equations with singular forces. The IIM was extended to the two-dimensional solution of the incompressible Navier-Stokes equations by Lee and LeVeque<sup>10</sup> and Lai and Li.<sup>11</sup> Jump conditions for velocity, pressure, and their derivatives for fluid flows in three spatial dimensions were derived by Xu and Wang.<sup>12</sup> Immersed interface methods developed by Thekkethil and Sharma<sup>13</sup> and Xu et al.<sup>14</sup> use level set representations of the geometry. In contrast, the IIM described by Kolahdouz<sup>15,16</sup> deals with interfaces represented as triangulated surfaces. Such surface representations can be readily used with finite element structural models.

A particularly challenging regime arises in fluid–structure interaction (FSI) problems involving thin layers of fluid between closely spaced interfaces. These scenarios are common in applications involving mechanical bearings, in which a thin fluid film lubricates relative motion between adjacent components. Resolving the dynamics in such narrow gaps is computationally expensive. Finite grid resolution limits the accuracy of interfacial interactions, and grid refinement quickly becomes prohibitive as the gap distance decreases. To address this, several studies have incorporated lubrication theory.<sup>17</sup> Fai and Rycroft<sup>18</sup> coupled lubrication models with the IB method, while Yacoubi et al.<sup>19</sup> integrated lubrication theory with an IIM by introducing analytic singular forces within the lubrication layer. These methods, however, have notable limitations. The IB-based approach is constrained by its smoothed force and velocity spreading operators, which generally reduce accuracy near immersed boundaries. Furthermore, the prior IIM-based approach uses cubic spline–based interface representations, which restricts its versatility compared to models that use piecewise linear elements, the standard in many engineering analyses. In addition, because these methods directly use lubrication theory, their implementations are complex and require prior knowledge of the immersed geometry's position, compared to a model which does not require an explicit lubrication model.

This paper presents an enhanced immersed interface method designed for simulating near-contact interactions between two interfaces using a novel bilinear velocity interpolation operator. When two interfaces lie within an interpolation stencil, the operator incorporates jump conditions from both interfaces to capture discontinuities in the velocity gradient. This enhanced interpolation yields substantially more accurate interface velocities and improves the accuracy of the Eulerian velocity field overall. Numerical experiments demonstrate notable improvements in velocity accuracy compared to prior lubrication theory approaches and show strong agreement with analytical solutions.

The primary contribution of this work is to establish that the enhanced IIM provides a robust and accurate framework for simulating fluid flows in thin fluid layers between multiple immersed interfaces. It captures interface and grid velocities accurately for separations as small as one-fiftieth of a grid cell and does so without requiring prior knowledge of interface orientation or separation distance.

# 2 Continuous Equations of Motion

This section outlines the equations of motion for a viscous incompressible fluid with interfacial forces concentrated on an immersed boundary. This boundary both applies force to the fluid and moves with the local fluid velocity. The fluid domain,  $\Omega$ , is partitioned into two subregions,  $\Omega_t^+$  (exterior) and  $\Omega_t^-$  (interior), by an interface  $\Gamma_t = \overline{\Omega_t^+} \cap \overline{\Omega_t^-}$ , as in Figure 1. We use the initial coordinates **X** 

of the boundary as Lagrangian coordinates, so that  $\mathbf{X} \in \Gamma_0$ , with corresponding current coordinates  $\chi(\mathbf{X}, t) \in \Gamma_t$ . The equations of motion are

$$\rho \frac{\mathrm{D}\mathbf{u}(\mathbf{x},t)}{Dt} = -\nabla p(\mathbf{x},t) + \mu \nabla^2 \mathbf{u}(\mathbf{x},t), \qquad \mathbf{x} \in \Omega,$$
 (1)

$$\nabla \cdot \mathbf{u}(\mathbf{x},t) = 0, \qquad \mathbf{x} \in \Omega, \tag{2}$$

$$\llbracket \mathbf{u}(\boldsymbol{\chi}(\mathbf{X},t),t) \rrbracket = 0, \qquad \mathbf{X} \in \Gamma_0, \tag{3}$$

$$\llbracket p(\mathbf{\chi}(\mathbf{X},t),t) \rrbracket = -j^{-1}(\mathbf{X},t) \mathbf{F}(\mathbf{X},t) \cdot \mathbf{n}(\mathbf{X},t), \qquad \mathbf{X} \in \Gamma_0, \tag{4}$$

$$\mu \left\| \frac{\partial \mathbf{u}(\boldsymbol{\chi}(\mathbf{X},t),t)}{\partial \mathbf{x}_i} \right\| = (\mathbb{I} - \mathbf{n}(\mathbf{X},t)\mathbf{n}(\mathbf{X},t)^{\mathsf{T}})j^{-1}(\mathbf{X},t)\mathbf{F}(\mathbf{X},t)n_i(\mathbf{X},t), \qquad \mathbf{X} \in \Gamma_0,$$
 (5)

$$\mathbf{U}(\mathbf{X},t) = \mathbf{u}(\boldsymbol{\chi}(\mathbf{X},t),t), \qquad \mathbf{X} \in \Gamma_0, \tag{6}$$

$$\frac{\partial \chi(\mathbf{X},t)}{\partial t} = \mathbf{U}(\mathbf{X},t), \qquad \mathbf{X} \in \Gamma_0, \tag{7}$$

in which  $\rho$ ,  $\mu$ ,  $\mathbf{u}(\mathbf{x},t)$ , and  $p(\mathbf{x},t)$  are the fluid's mass density, dynamic viscosity, velocity, and pressure.  $\mathbf{F}(\mathbf{X},t)$  and  $\mathbf{U}(\mathbf{X},t)$  are the interfacial force and velocity, respectively, in Lagrangian material coordinates, and  $\mathbf{n}(\mathbf{X},t)$  is the surface normal vector in the interface's current configuration.  $\mathbf{J}^{-1} = \frac{\mathrm{d}a}{\mathrm{d}A}$  relates surface area along the interface in the current (da) and reference (dA) configurations. For rigid body motions,  $\mathbf{J}^{-1} = 1$ . The jump conditions express the discontinuity in fluid traction generated by the singular force along the interface. For a general function  $\phi(\mathbf{x},t)$  and position  $\mathbf{x} = \chi(\mathbf{X},t)$  along the interface, the jump condition is

$$\llbracket \phi(\mathbf{x},t) \rrbracket \equiv \phi^{+}(\mathbf{x},t) - \phi^{-}(\mathbf{x},t) \equiv \lim_{\epsilon \to 0^{+}} \phi(\mathbf{x} + \epsilon \mathbf{n}(\mathbf{X},t),t) - \lim_{\epsilon \to 0^{-}} \phi(\mathbf{x} - \epsilon \mathbf{n}(\mathbf{X},t),t). \tag{8}$$

Equations (3)–(5) were derived in previous work by Lai and Li,<sup>11</sup> Xu and Wang,<sup>12</sup> and Peskin and Printz.<sup>20</sup> Our numerical tests consider cases with both stationary and moving boundaries. Both cases involve forces that are computed using a penalty method. In either case, we view the boundary as having a *prescribed* configuration  $\xi(X,t)$  and an *actual* configuration  $\chi(X,t)$ . These two configurations are connected through penalty forces that are of the form

$$\mathbf{F}(\mathbf{X},t) = \kappa(\boldsymbol{\xi}(\mathbf{X},t) - \boldsymbol{\gamma}(\mathbf{X},t)),\tag{9}$$

in which  $\kappa$  is the penalty spring stiffness. As  $\kappa \to \infty$ , this constraint exactly imposes the motion.<sup>21</sup> This study considers some stationary interfaces, so that  $\chi(X,t) = X$ . The simplified force model becomes  $F(X,t) = \kappa(X-\chi(X,t))$ . Because the total interface displacement in our numerical experiments is between two to three orders of magnitude smaller than the domain length, we use X to mediate the coupling between the interface and the fluid without loss of accuracy.

# 3 Discrete Equations of Motion

This section describes the spatial and temporal discretizations of the equations of motion. It also details our modified velocity interpolation which accounts for multiple interfaces in one grid cell. We also describe the projection of the discrete jump conditions a continuous basis, and the discrete force spreading operator.

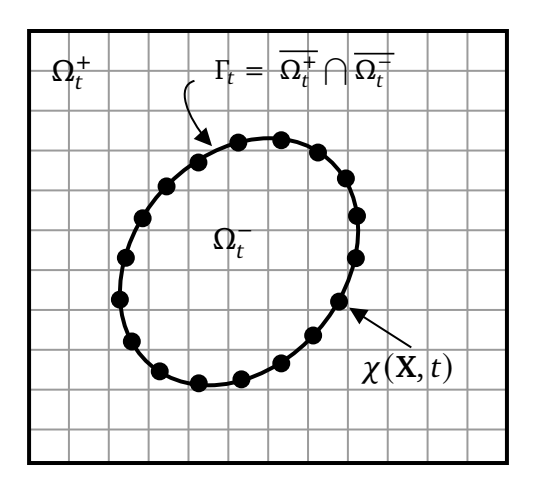


**Figure 1**: A Lagrangian coordinate system represents represents the interface,  $\Gamma_t$ . At time t, the position of the interface in Eulerian coordinates is  $\gamma(X, t)$ .

#### 3.1 Interface Representation

We use a finite element representation of the immersed interface with triangulation  $\mathcal{T}_h$  of  $\Gamma_0$ , the reference configuration. Consider elements  $U_i$  such that  $\mathcal{T}_h = \bigcup_i U_i$ , with i indexing the mesh elements. The nodes of the mesh elements are  $\{\mathbf{X}_j\}_{j=1}^M$  and have corresponding nodal (Lagrangian) basis functions  $\{\psi_j(\mathbf{X})\}_{j=1}^M$ . Herein, we consider piecewise linear interface representations, in which  $\psi_j$  is a piecewise linear Lagrange polynomial. The nodal basis functions  $\psi_j(\mathbf{X})$  are continuous across elements but are not differentiable at the nodes. The current location of the interfacial nodes at time t are  $\{\chi_j(t)\}_{j=1}^M$ . In the finite element space dictated by the subspace  $S_h = \mathrm{span}\{\psi_j(\mathbf{X})\}_{j=1}^M$ , the configuration of the interface is  $\chi_h(\mathbf{X},t) = \sum_{i=1}^M \chi_j(t) \psi_j(\mathbf{X})$ .

#### 3.2 Projected Jump Conditions

Jump conditions must be evaluated at arbitrary positions along the interface to evaluate the forcing terms associated with stencils that cut the interface. If using the normal vectors determined directly from the  $C^0$  interface representation, Eq. (10), pointwise expressions for the jump conditions for pressure, Eq. (3), and shear stress, Eq. (4), are discontinuous between elements. To obtain a continuous representation of these jump conditions along the discretized boundary geometry, previous work by Kolahdouz et al. <sup>15</sup> projected both pressure and shear stress jump conditions onto the same finite element basis used to represent the geometry. For example, the pressure jump condition in the continuous Lagrangian basis is

$$[\![p]\!]_h(\mathbf{X},t) = \sum_{j=1}^M [\![p]\!]_j(t) \, \psi_j(\mathbf{X}),$$
 (10)

in which  $[\![p]\!]_j(t)$  is the jump condition at a particular Lagrangian nodes at time t. Projecting the pressure jump condition requires  $[\![p]\!]_h(\mathbf{X},t)$  to satisfy

$$\int_{\Gamma_0} \llbracket p \rrbracket_h(\mathbf{X}, t) \, \psi_j(\mathbf{X}) \, \mathrm{d}A = \int_{\Gamma_0} j^{-1}(\mathbf{X}, t) \, \mathbf{F}_h(\mathbf{X}, t) \cdot \mathbf{n}(\mathbf{X}, t) \, \psi_j(\mathbf{X}) \mathrm{d}A, \forall j = 1, \dots, M.$$
 (11)

The projection of  $[\![\frac{\partial u(\chi(X,t),t)}{\partial x_i}]\!]$  is handled similarly. In this work, we evaluate these integrals using a seventh order Gaussian quadrature scheme.

#### 3.3 Modified Velocity Interpolation

The configuation of the Lagrangian mesh is updated by applying the no slip condition  $\mathbf{U}_h = \Im[X, \mathbf{F}](\mathbf{u})$ , in which  $\Im$  is a modified bilinear interpolation in two spatial dimesions and subsequent  $L^2$  projection of  $\mathbf{U}_h$  into the subspace  $S_h$ . For simplicity of notation, the subscript h is omitted in this section.

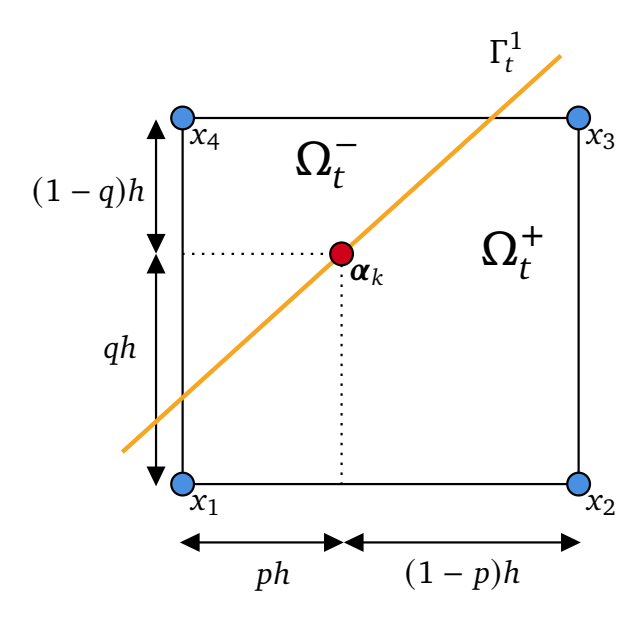


**Figure 2:** Velocity interpolation from Cartesian grid velocities (blue) to quadrature point  $\alpha_k$  (red) on  $\Gamma_t^1$ . Velocities at  $x_1$ ,  $x_2$ , and  $x_3$  require correction terms to account for the discontinuity in the velocity gradient generated by the interface.

This section explores the modified interpolation step, as the  $L^2$  projection is the same as used in Kolahdouz et al.<sup>15</sup> Consider the bounding box of Eulerian nodes on which Cartesian velocities are evaluated. First, we identify all interfacial quadrature points,  $\{\alpha_k\}_{k=1}^N$ , on  $\Gamma_t^1$  that are located within the bounding box. If  $\Gamma_t^1$  is the only interface within this box, we compute a modified bilinear interpolation of the corner velocities to  $\alpha_k$  using correction terms, as in Tan et al.<sup>22</sup> For an isotropic grid spacing h, the interface velocity  $\mathbf{U}(\alpha_k)$  is

$$\mathbf{U}(\boldsymbol{\alpha}_k) = (1-p)(1-q)(\mathbf{u}_1 + \mathbf{C}_1) + p(1-q)(\mathbf{u}_2 + \mathbf{C}_2) + pq(\mathbf{u}_3 + \mathbf{C}_3) + (1-p)q(\mathbf{u}_4 + \mathbf{C}_4), \quad (12)$$

in which

$$\mathbf{C}_{1} = \begin{cases} -hp \left[ \left[ \frac{\partial \mathbf{u}(\boldsymbol{\alpha}_{k}, t)}{\partial x} \right] \right] - hq \left[ \left[ \frac{\partial \mathbf{u}(\boldsymbol{\alpha}_{k}, t)}{\partial y} \right] \right], & \mathbf{x} \in \Omega_{t}^{+}, \\ 0, & \mathbf{x} \in \Omega_{t}^{-}, \end{cases}$$
(13)

$$\mathbf{C}_{2} = \begin{cases} h(1-p) \left[ \left[ \frac{\partial \mathbf{u}(\boldsymbol{\alpha}_{k},t)}{\partial x} \right] - hq \left[ \left[ \frac{\partial \mathbf{u}(\boldsymbol{\alpha}_{k},t)}{\partial y} \right] \right], & \mathbf{x} \in \Omega_{t}^{+}, \\ 0, & \mathbf{x} \in \Omega_{t}^{-}, \end{cases}$$

$$(14)$$

$$\mathbf{C}_{3} = \begin{cases} h(1-p) \left[ \left[ \frac{\partial \mathbf{u}(\boldsymbol{\alpha}_{k},t)}{\partial x} \right] \right] + h(1-q) \left[ \left[ \frac{\partial \mathbf{u}(\boldsymbol{\alpha}_{k},t)}{\partial y} \right] \right], & \mathbf{x} \in \Omega_{t}^{+}, \\ 0, & \mathbf{x} \in \Omega_{t}^{-}, \end{cases}$$
(15)

$$\mathbf{C}_{4} = \begin{cases} -hp \left[ \left[ \frac{\partial \mathbf{u}(\boldsymbol{\alpha}_{k}, t)}{\partial x} \right] \right] + h(1 - q) \left[ \left[ \frac{\partial \mathbf{u}(\boldsymbol{\alpha}_{k}, t)}{\partial y} \right] \right], & x \in \Omega_{t}^{+}, \\ 0, & x \in \Omega_{t}^{-}, \end{cases}$$
(16)

are correction terms account for the discontinuities in the fluid's shear stress generated by the interface. Figure 2 provides a schematic in which  $x_1$ ,  $x_2$ , and  $x_3$  are Cartesian velocity nodes that contribute to the correction terms.

When a second interface,  $\Gamma_t^2$ , lies in the same bounding box as  $\Gamma_t^1$ , additional correction terms are added to account for the discontinuity in shear stress generated by  $\Gamma_t^2$ . We cast rays,  $\{\mathbf{r}_i\}_{i=1}^4$ , from  $\alpha_k$  to each corner of the bounding box and locate any intersection points,  $\tilde{\mathbf{x}}_i$ , on the second interface. Next, we evaluate  $\left[\!\!\left[\frac{\partial \mathbf{u}(\tilde{\mathbf{x}}_i,t)}{\partial \mathbf{x}}\right]\!\!\right]$  by interpolating the jump condition from neighboring Lagrangian nodes on the element where  $\tilde{\mathbf{x}}_i$  is located. Then, we add a second correction term to the modified bilinear interpolation:

$$\tilde{\mathbf{C}}_{i} = \begin{cases}
\operatorname{sign}(\mathbf{r}_{i}^{x}) \, \xi_{i} \left[ \left[ \frac{\partial \mathbf{u}(\tilde{\mathbf{x}}_{i}, t)}{\partial x} \right] \right] + \operatorname{sign}(\mathbf{r}_{i}^{y}) \, \zeta_{i} \left[ \left[ \frac{\partial \mathbf{u}(\tilde{\mathbf{x}}_{i}, t)}{\partial y} \right] \right], & \exists \, \tilde{\mathbf{x}}_{i} \in \Gamma_{t}^{2}, \\
0, & \text{otherwise,}
\end{cases} \tag{17}$$

in which weights  $\xi_i$  and  $\zeta_i$  are the components unsigned distances from  $\tilde{\mathbf{x}}_i$  to the corner of the bounding box, and  $r_i^x$  and  $r_i^y$  are the components of  $\mathbf{r}_i$ . Figure 3 shows a schematic of the ray casting and jump condition weights  $\xi_i$  and  $\zeta_i$ .

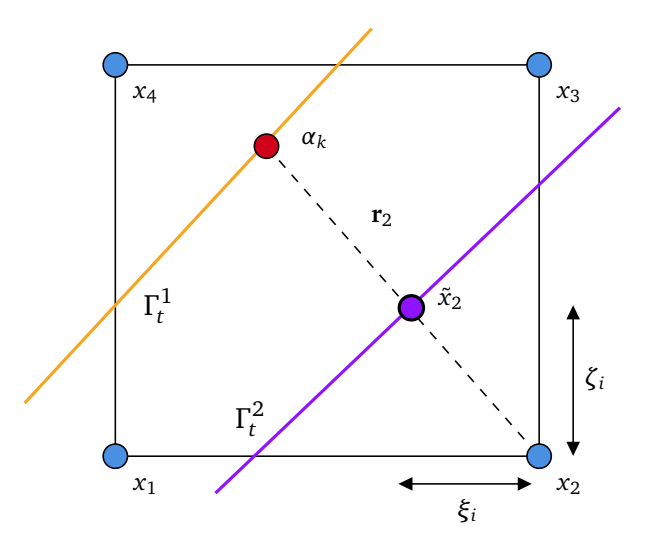


**Figure 3:** Schematic for velocity interpolation when two interfaces lie within the same bounding box. Weights  $\xi$  and  $\zeta$  are the x and y components of the unsigned distance from  $\tilde{\mathbf{x}}_2$  to  $\mathbf{x}_2$ .

Last, we compute the modified velocity interpolation at each  $\alpha_k$ . The two correction modified interpolation scheme is

$$U(\boldsymbol{\alpha}_{k}) = (1-p)(1-q)(\mathbf{u}_{1} + \mathbf{C}_{1} + \tilde{\mathbf{C}}_{1}) + p(1-q)(\mathbf{u}_{2} + \mathbf{C}_{2} + \tilde{\mathbf{C}}_{2}) + pq(\mathbf{u}_{3} + \mathbf{C}_{3} + \tilde{\mathbf{C}}_{3}) + (1-p)q(\mathbf{u}_{4} + \mathbf{C}_{4} + \tilde{\mathbf{C}}_{4}).$$
(18)

Figure 4 shows all of the elementary orientations in which two interfaces can arise in one bounding box. Other orientations can be achieved by  $\frac{\pi}{2}$  rotations and swapping the positions of  $\Gamma^1_t$  and  $\Gamma^2_t$ .

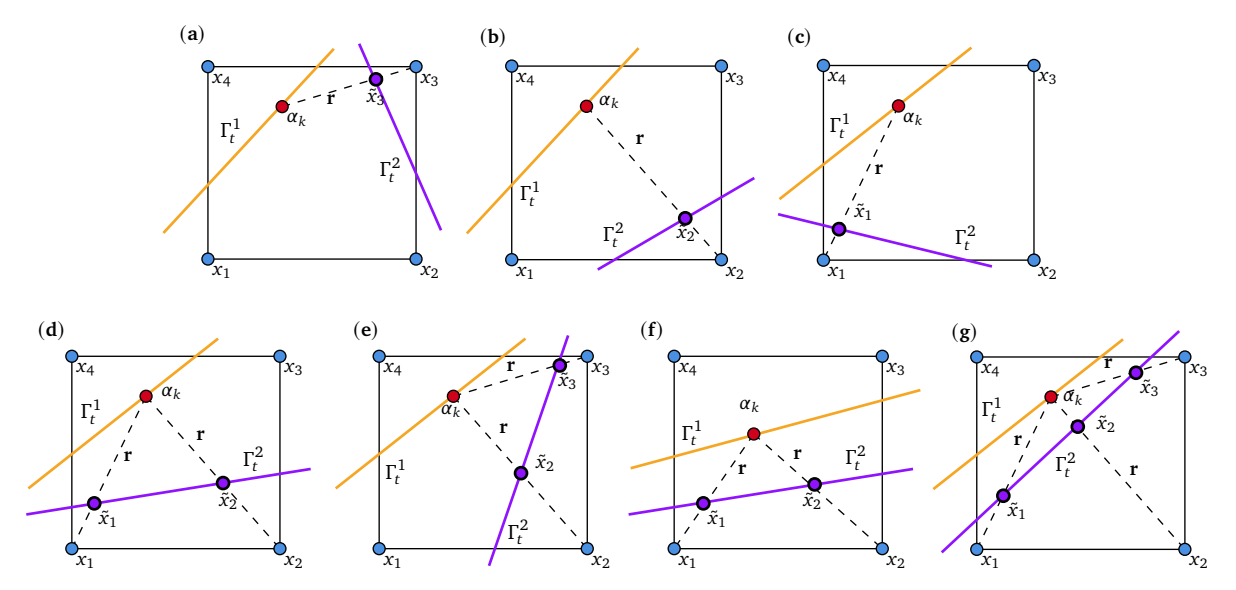


**Figure 4:** Velocity interpolation schematics are shown for various orientations of  $\Gamma^1_t$  and  $\Gamma^2_t$  when both interfaces lie within one grid cell. The intersection of ray  $\mathbf{r}$  with  $\Gamma^2_t$  is denoted by  $\tilde{x}$ . Panels (a)-(c) show the possible orientations when  $\Gamma^1_t$  and  $\Gamma^2_t$  each isolate one node. Panels (d) and (e) show the possible orientations when  $\Gamma^1_t$  isolates one node and  $\Gamma^2_t$  isolates two nodes. Panel (f) shows the orientation in which both  $\Gamma^1_t$  and  $\Gamma^2_t$  isolate two nodes. Panel (g) shows the orientation in which  $\Gamma^1_t$  isolates one node and  $\Gamma^2_t$  isolates three nodes. All other possible orientations can be achieved by rotating both interfaces and swapping  $\Gamma^1_t$  with  $\Gamma^2_t$ .

Finally, these interpolated velocities are then used to compute the  $L^2$  projection of the velocity at mesh nodes, as in Kolahdouz et al. These nodal velocities are represented in the finite element basis as  $\mathbf{U}_h(\mathbf{X},t) = \sum_{j=1}^M \mathbf{U}_j(t) \, \psi_j(\mathbf{X})$ .

## 3.4 Finite Difference Approximation

We use a staggered-grid discretization of the incompressible Navier-Stokes equations. The discretization approximates pressure at cell centers, and velocity and forcing terms at the center of cell edges. Our computations use an isotropic grid, such that  $h = \Delta x = \Delta y$ . We use second-order accurate finite difference stencils, and define the discrete divergence of the velocity  $\mathbf{D} \cdot \mathbf{u}$  on cell centers, and the discrete pressure gradient  $\mathbf{G}p$  and discrete Laplacian  $L\mathbf{u}$  on cell edges. Finite difference stencils that cut through the interface require additional forcing terms, which are commonly referred to as correction terms, to account for discontinuities in the pressure and velocity gradients, as in previous work. Is

## 3.5 Force Spreading

The spreading operator,  $S[\chi(X,t)]$ , relates the Lagrangian force  $F_h(X,t) = \sum_{j=1}^M F_j(t) \psi_j(X)$  to the Eulerian forces f on the Cartesian grid by summing all correction terms in the modified finite difference stencils involving the Lagrangian force. Correction terms, which are detailed in previous work, depend on the projected jump conditions, as computed in Section 3.2.

#### 3.6 Time Integration

Each step begins with known values of  $\chi^n$  and  $\mathbf{u}^n$  at time  $t^n$ , and  $p^{n-\frac{1}{2}}$  at time  $t^{n-\frac{1}{2}}$ . The goal is to compute  $\chi^{n+1}$ ,  $\mathbf{u}^{n+1}$ , and  $p^{n+\frac{1}{2}}$ . First, an initial prediction of the structure location at time  $t^{n+1}$  is determined by

$$\frac{\widehat{\chi}^{n+1} - \chi^n}{\Lambda t} = \mathbf{U}^n(\chi^n) = \mathfrak{I}[\chi^n, \mathbf{F}^n](\mathbf{u}^n).$$
(19)

We can then approximate the structure location at time  $t^{n+\frac{1}{2}}$  by

$$\chi^{n+\frac{1}{2}} = \frac{\widehat{\chi}^{n+1} + \chi^n}{2}.$$
 (20)

Next, we solve for  $\mathbf{u}^{n+1}$  and  $p^{n+\frac{1}{2}}$  in which  $\mathbf{f}^{n+\frac{1}{2}} = \mathbb{S}[\boldsymbol{\chi}^{n+\frac{1}{2}}]\mathbf{F}(\boldsymbol{\chi}^{n+\frac{1}{2}},t^{n+\frac{1}{2}})$ :

$$\rho\left(\frac{\mathbf{u}^{n+1} - \mathbf{u}^n}{\Delta t} + \mathbf{A}^{n+\frac{1}{2}}\right) = -\mathbf{G}p^{n+\frac{1}{2}} + \mu L\left(\frac{\mathbf{u}^{n+1} + \mathbf{u}^n}{2}\right) + \mathbf{f}^{n+\frac{1}{2}},\tag{21}$$

$$\mathbf{D} \cdot \mathbf{u}^{n+1} = 0, \tag{22}$$

in which the non-linear advection term,  $\mathbf{A}^{n+\frac{1}{2}} = \frac{3}{2}\mathbf{A}^n - \frac{1}{2}\mathbf{A}^{n-1}$ , is handled with the xsPPM7 variant<sup>25</sup> of the piecewise parabolic method.<sup>26</sup>  $\mathbf{G}, \mathbf{D} \cdot$ , and L are the discrete gradient, divergence, and Laplacian operators. The system of equations is iteratively solved via the FGMRES algorithm with the projection method preconditioner.<sup>24</sup> Last, we update the structure's location,  $\chi^{n+1}$ , with

$$\frac{\chi^{n+1} - \chi^n}{\Delta t} = \mathbf{U}^{n+\frac{1}{2}} = \Im[\chi^{n+\frac{1}{2}}, \mathbf{F}^{n+\frac{1}{2}}] \left(\frac{\mathbf{u}^n + \mathbf{u}^{n+1}}{2}\right).$$
 (23)

## 3.7 Software Implementation

All computations for were completed through IBAMR,<sup>27</sup> which utilizes parallel computing libraries and adaptive mesh refinement (AMR). IBAMR uses other libraries for setting up meshes, fast linear algebra solvers, and postprocessing, including SAMRAI,<sup>28</sup> PETSc,<sup>29–31</sup> *hypre*,<sup>32,33</sup> and libMesh.<sup>34,35</sup>

# 4 Numerical Experiments

We first use shearing parallel plates as a benchmark case to examine the accuracy of our two correction algorithm on a globally piecewise linear velocity field, for which our interfacial velocity recreation should be exact. We also examine benchmark studies in which the velocity field is non-linear in x and y, particularly two concentric rotating cylinders. This benchmark highlights our method's robust approach to treating two intersections and computing secondary correction terms at a variety of orientations. Next, we examine the reconstructed interfacial velocity field on two eccentric rotating cylinders. This study examines geometries in which symmetry is broken along one axis. Both the concentric and eccentric cylinders are tested for accuracy for minimal separation distances  $\Delta s = \frac{h}{10}$ . We impose rigid body motions using a penalty method described in Section 2. Because the penalty parameter is finite, generally there are discrepancies between the prescribed and actual positions of the interface. In numerical tests, we choose  $\kappa$  to ensure that the discrepancy in interface configurations  $\epsilon_X = \|\xi(X,t) - \chi(X,t)\|$  satisfies  $\epsilon_X < \frac{h}{10}$ .

#### 4.1 Shearing Parallel Plates

This section considers the flow between two shearing parallel plates in two spatial dimensions. The plates are aligned with the x-axis, such that the top plate lies at  $y=\frac{1}{48}$  and the bottom plate lies at  $y=-\frac{1}{48}$ . The distance between the plates is  $\Delta s=\frac{1}{24}$ . The two plates extend to the left and right ends of the computational domain,  $\Omega=[-1,1]^2$ . Figure 4 shows a schematic for the model's setup. The top plate moves to the right at a velocity of 0.003125, and the bottom plate moves to the left at a velocity of -0.003125. We set  $\rho=1$  and  $\mu=0.02$ . The domain is discretized into N=16, 32, and 64 cells in both directions such that the mesh spacing is h=0.125, 0.0625, and 0.03125 respectively. We set the Lagrangian mesh width to be twice as coarse as the background Cartesian grid spacing. The time step size  $\Delta t$  scales with h such that  $\Delta t=\frac{h}{100}$ . Periodic boundary conditions are used on each side. For this time step size and grid spacing, the Courant-Friedrichs-Lewy (CFL) number is approximately  $1.7 \cdot 10^{-5}$  once the model reaches steady state. To impose rigid body motion, we set  $\kappa = C_{\kappa}(\frac{N}{8})^2$  with  $C_{\kappa} = 12.0$ . Figure 5 shows a schematic for the shearing plates setup.

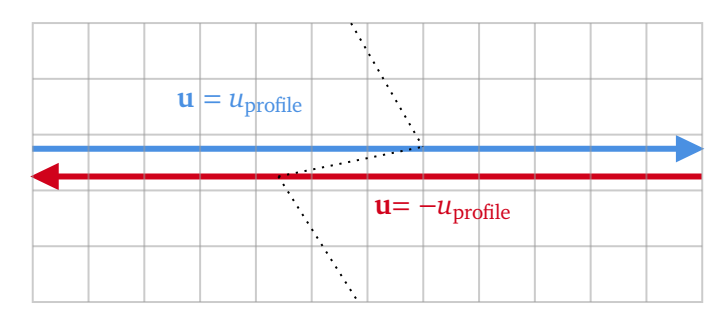
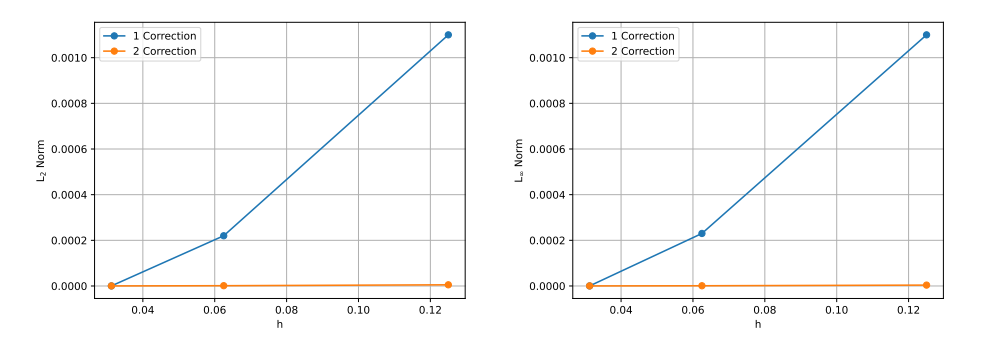


Figure 5: Shearing parallel plate schematic. Both plates move with equal and opposite velocity.

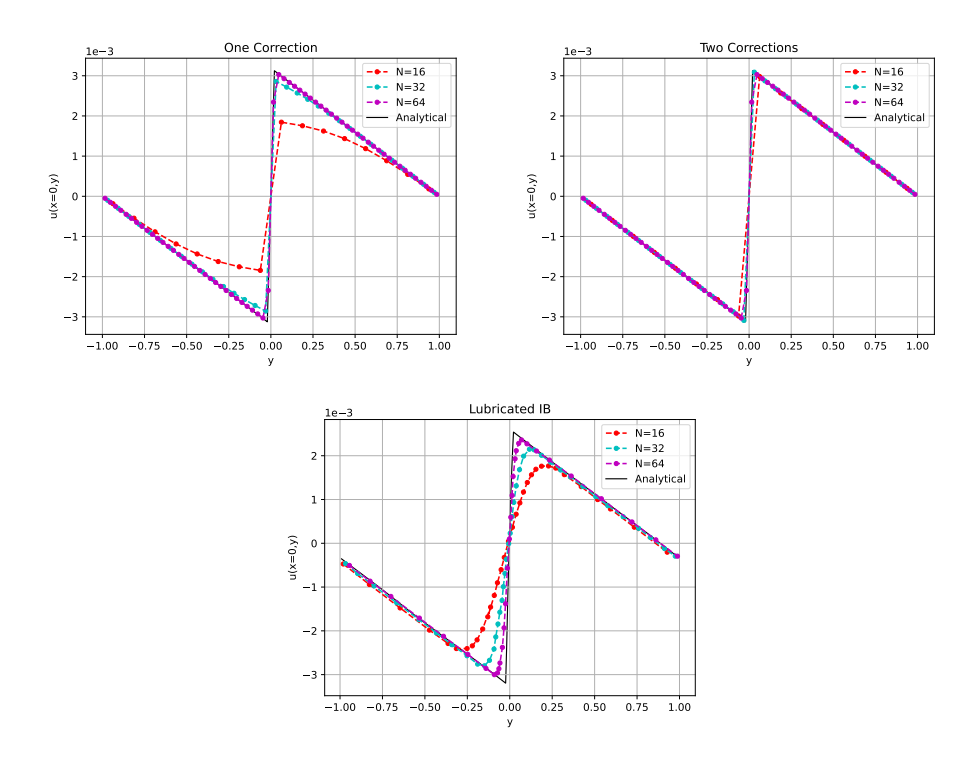
We compare the  $L^2$  and  $L^{\infty}$  errors of the Eulerian fluid x-velocity, for both of the one and two correction methods at each grid resolution in Figure 6.



**Figure 6:** Convergence of the shearing parallel plates' velocity in the  $L^2$  and  $L^\infty$  norms. Both methods'  $L^2$  and  $L^\infty$  errors converge to within machine precision of each other at the finest grid resolution, in which the  $\Delta s > h$  and only one interface cuts each stencil. The two correction method exhibits similar error at each grid resolution, approximately  $10^{-6}$ , due to the finite Stokes solver tolerance.

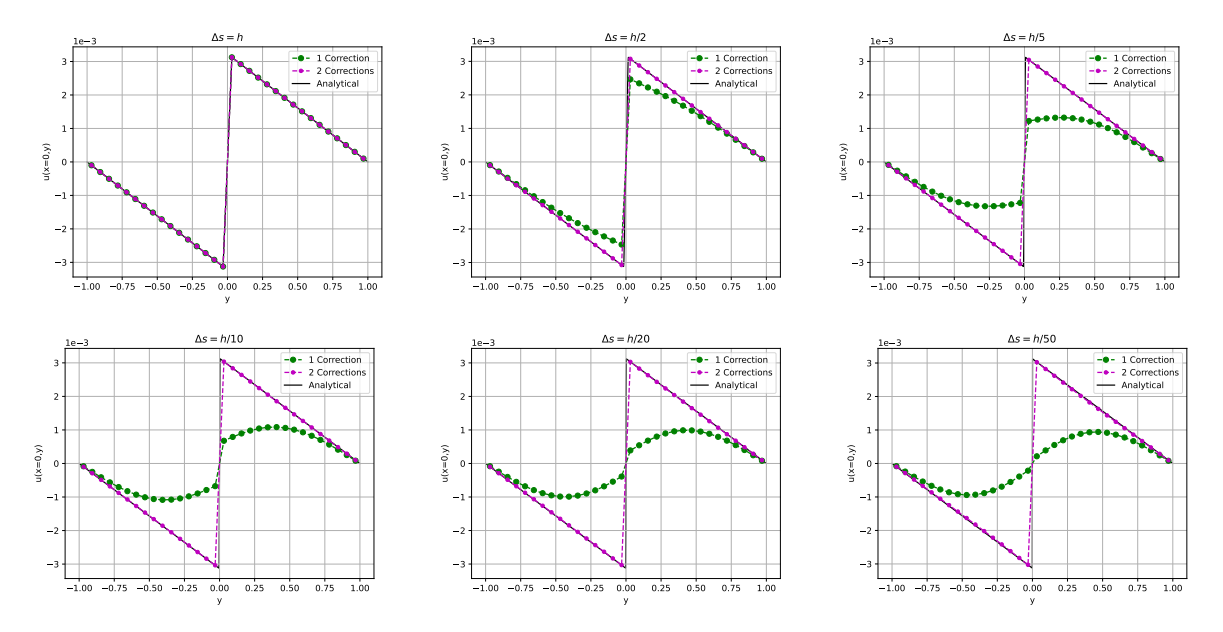
We compare the accuracy of the present one and two correction methods with Fai and Rycroft's<sup>18</sup> lubricated IB method. We compute the Eulerian velocity profile along the line x = 0 and compare it

to the analytical solution in Figure 7. For N = 16 and 32 grid cells,  $\Delta s < h$ . Both correction methods demonstrate convergence under grid refinement. The two correction algorithm results in substantially more accuracy at coarser grid resolutions than the one correction and lubricated IB method.



**Figure 7:** Convergence of the pointwise accuracy of the velocity profile u(x = 0, y) across parallel plates. Our present two correction method is compared to the previous one correction method and the results taken from Fai and Rycroft's lubricated IB method.<sup>18</sup> Both correction methods converge under grid refinement, and the two correction algorithm is substantially more accurate at coarser Cartesian grid resolutions than both one correction and the lubricated IB method.

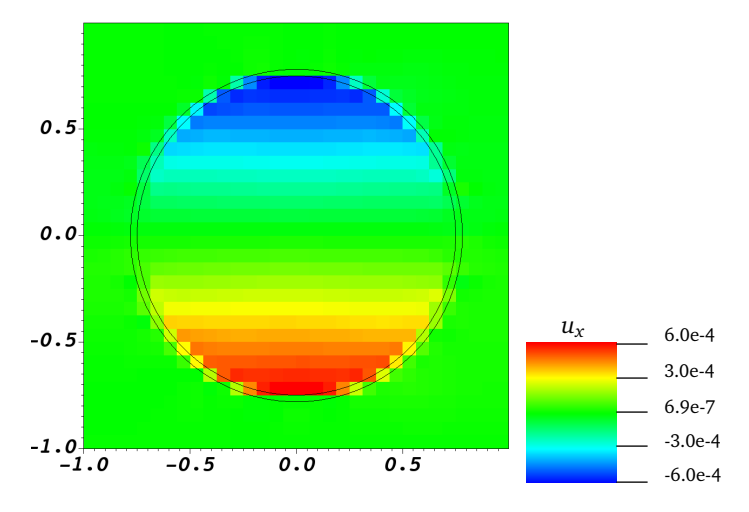
To assess the accuracy of our method in the limit as the distance between the interfaces,  $\Delta s$ , approaches zero, we conduct an interface convergence test. Fixing the Cartesian grid resolution at N=32 grid cells in each direction, we set  $\Delta s=h,\frac{h}{2},\frac{h}{5},\frac{h}{10},\frac{h}{20}$ , and  $\frac{h}{50}$ . Figure 8 compares the velocity profile u(x=0,y) using the one and two correction methods. At all separation distances, the one correction method clearly suffers from decreased accuracy as  $\Delta s \to 0$ , while the two correction method shows excellent agreement with the analytical velocity profile.



**Figure 8:** Comparison of the velocity profile u(x=0,y) for various separations between two shearing parallel plates. When  $\Delta s < h$ , the two correction method demonstrates substantially more accurate than the one correction method, even when  $\Delta s = \frac{h}{50}$ .

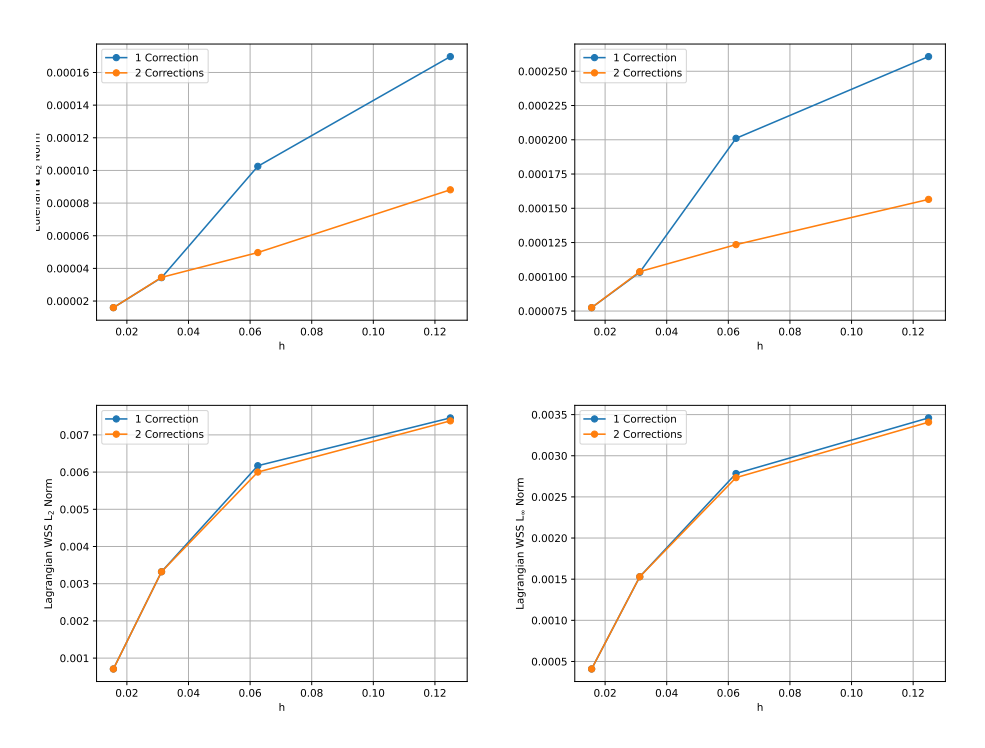
## 4.2 Concentric Rotating Cylinders

This section considers the flow between two concentric rotating cylinders in two spatial dimensions. The cylinders are centered at the origin, with radii  $R_{\rm inner}=0.75$  and  $R_{\rm outer}=0.78125$ , such that the separation of the interfaces is  $\Delta s=0.03125$ . The outer cylinder is fixed in place, and the inner cylinder rotates counter-clockwise at a rotational velocity  $\omega=8.33\cdot 10^{-4}$ . The fluid domain is  $\Omega=[-1,1]^2$ . Figure 9 shows a schematic for the model's setup. We set  $\rho=1$  and  $\mu=0.2$ . The domain is discretized into N=16, 32, 64, and 128 cells in both directions such that the mesh spacing is h=0.125, 0.0625, 0.03125, and 0.015625 respectively. We set the Lagrangian mesh width to be equal to the background Cartesian grid spacing. The time step size  $\Delta t$  scales with h such that  $\Delta t=\frac{h}{100}$ . We use zero normal traction and zero tangential velocity boundary conditions on each side of the computational domain. For this time step size and these grid spacings, the CFL number is approximately  $10^{-6}$  once the model reaches steady state. To impose rigid body motion, we set  $\kappa=\frac{C_\kappa}{(\Delta t)^2}$  with  $C_\kappa=2.0\cdot 10^{-4}$ .



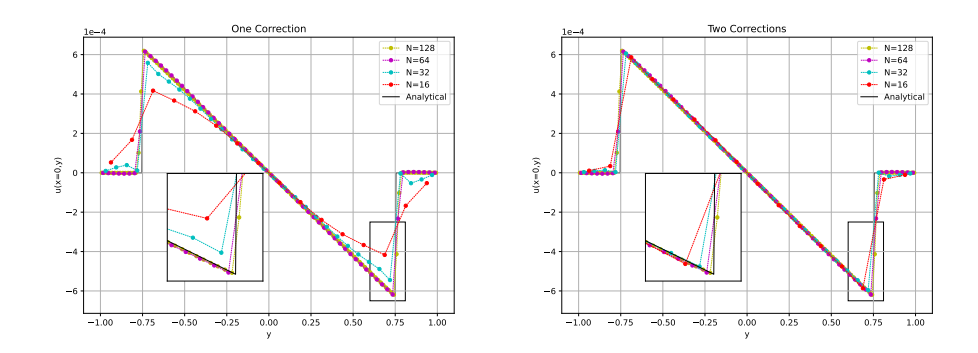
**Figure 9:** The *x*-component of the velocity field is visualized over the entire fluid domain at t = 5 using the two correction method. N = 32 grid cells are used in either direction, such that  $\Delta s = \frac{h}{2}$ .

We compare the convergence of  $\mathbf{u}$  and the the Lagrangian wall shear stress (WSS) under grid refinement in Figure 10. At all grid resolutions in which  $\Delta s < h$ , the two correction method shows increased accuracy compared to the previous one correction method. When  $\Delta s \geq h$ , however, the interface velocity interpolation stencil intersects the interfaces only once, and the two formulations yield identical results.



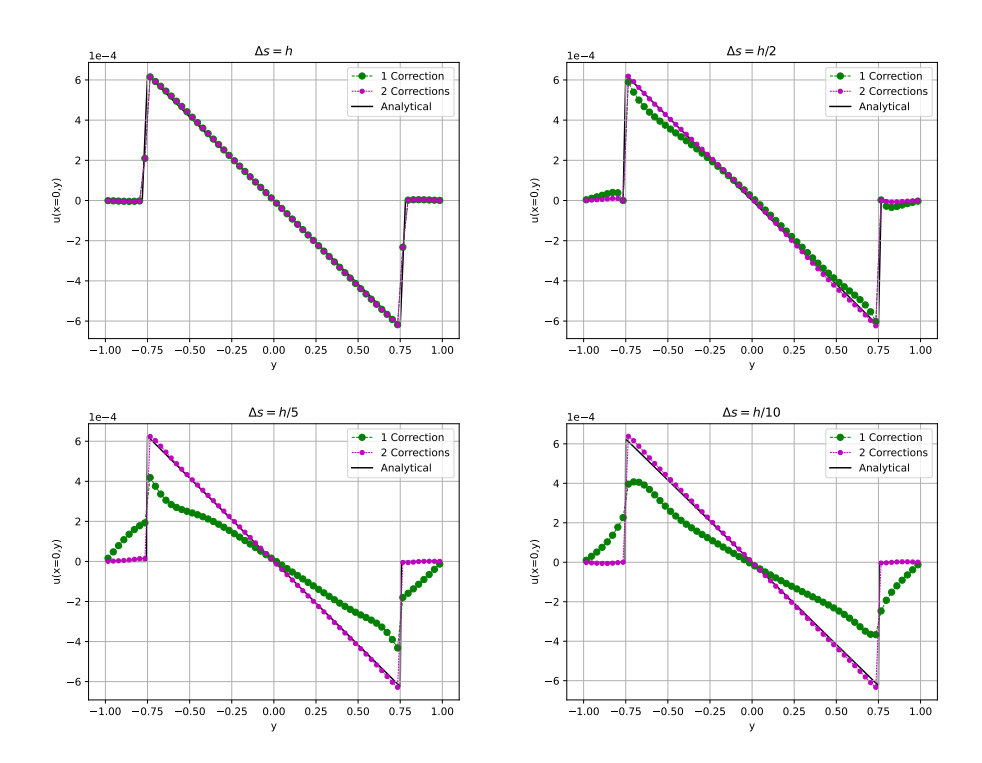
**Figure 10:** Convergence of  $\mathbf{u}$  and Lagrangian wall shear stress for concentric rotating cylinders. Our present two correction method is compared to the previous one correction method. Both methods converge under grid refinement, and the two correction algorithm is more accurate at coarser grid resolutions than the one correction method.

We compute the u(x = 0, y) profile from y = -1 to y = 1 for both one and two correction methods, and compare their convergence properties in Figure 11. The one correction method demonstrates reduced accuracy near the interfaces in near contact, whereas the two correction method shows excellent agreement with the analytical velocity profile.



**Figure 11:** Convergence of the pointwise accuracy of the velocity profile u(x = 0, y) across concentric rotating cylinders. Our present two correction method is compared to the previous one correction method. Both correction methods converge under grid refinement, and the two correction algorithm is significantly more accurate at coarser Cartesian grid resolutions than the one correction method.

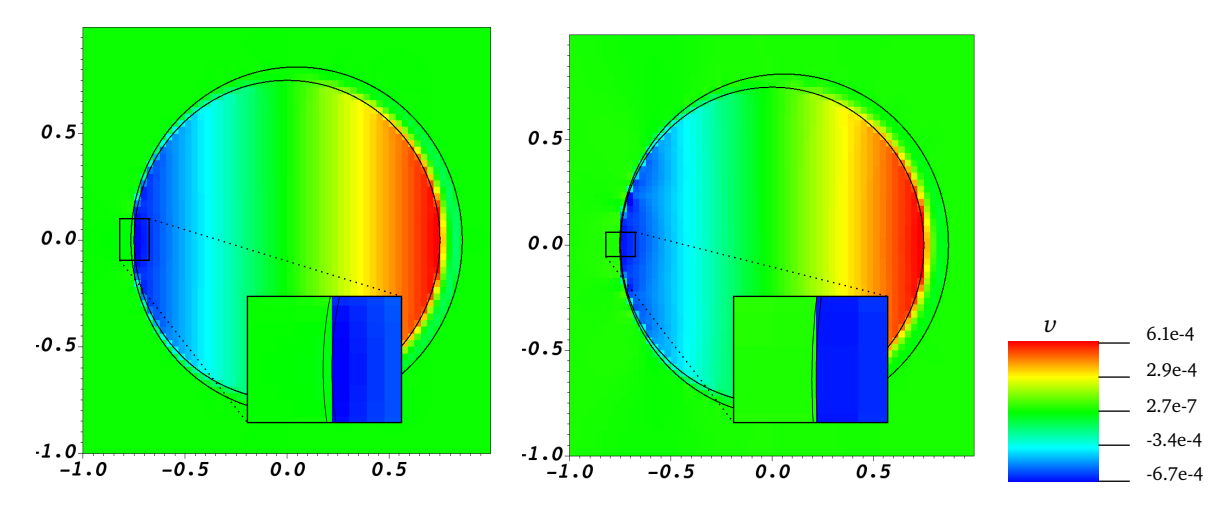
Last, we analyze the accuracy of the two methods for various separation distances between the cylinders in Figure 12. We fix the Cartesian grid resolution using N=64 grid cells in each direction. We vary  $\Delta s$  between the two cylinders, particularly h,  $\frac{h}{2}$ ,  $\frac{h}{5}$ , and  $\frac{h}{10}$ . When  $\Delta s < h$ , the one correction method clearly suffers from decreased accuracy throughout the computational domain. In contrast, the two correction method maintains substantially better agreement with the analytical profile, even when  $\Delta s = \frac{h}{10}$ .



**Figure 12:** Comparison of the velocity profile  $u_x(x = 0, y)$  for various separations between two concentric rotating cylinders. When  $\Delta s < h$ , the two correction method is substantially more accurate than the one correction method.

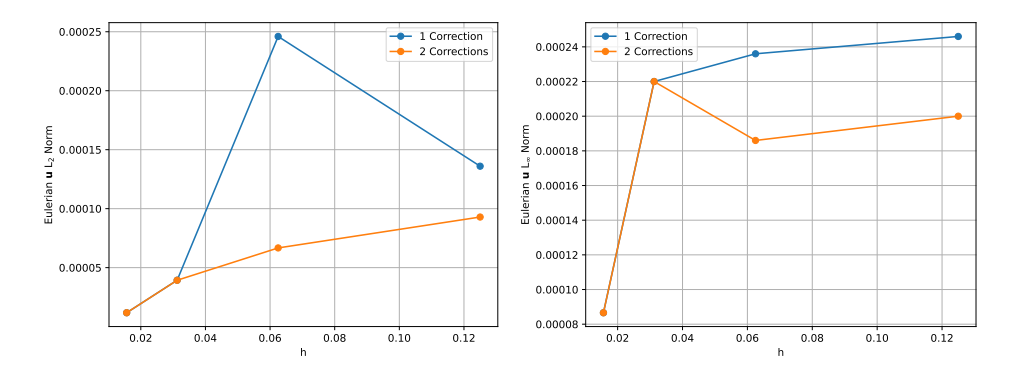
## 4.3 Eccentric Rotating Cylinders

This section considers the flow between two eccentric rotating cylinders in two spatial dimensions. The inner cylinder is centered at the origin, with radii  $R_{\rm inner}=0.75$ , whereas the outer cylinder is centered at (e,0)=(0.03125,0) and  $R_{\rm outer}=0.8125$ . The outer cylinder is fixed in place, and the inner cylinder rotates counter-clockwise at a rotational velocity  $\omega=8.33\cdot 10^{-4}$ . The fluid domain is  $\Omega=[-1,1]^2$ . Figure 13 shows a schematic for the model's setup. We set  $\rho=1$  and  $\mu=0.2$ . The domain is discretized into N=16,32,64, and 128 cells in both directions such that the mesh spacing is h=0.125,0.0625,0.03125, and 0.015625 respectively. We set the Lagrangian mesh width to be equal to the background Cartesian grid spacing. The time step size  $\Delta t$  scales with h such that  $\Delta t=\frac{h}{100}$ . We use zero normal traction and zero tangential velocity boundary conditions on each side. For this time step size and these grid spacings, the CFL number is approximately  $10^{-6}$  once the model reaches steady state. To impose rigid body motion, we set  $\kappa=\frac{C_\kappa}{(\Delta t)^2}$ , in which  $C_\kappa=2.0\cdot 10^{-4}$ .



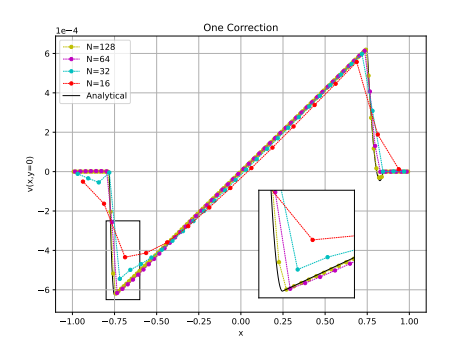
**Figure 13:** The *y*-component of the velocity field for two eccentric rotating cylinders is visualized over the entire fluid domain at t = 5 using the two correction method. The left panel has a minimal  $\Delta s$  of  $\frac{h}{2}$ , and the right panel has a minimal  $\Delta s$  of  $\frac{h}{10}$ . N = 64 grid cells are used in either direction.

We compare the convergence of  $\mathbf{u}$  under grid refinement in both the  $L^2$  and  $L^\infty$  norms in Figure 14. For grid resolutions in which  $\Delta s < h$ , the one two correction method demonstrates substantially less error. For grid resolutions in which  $\Delta s \ge h$ , the interface velocity interpolation stencil intersects the interfaces only once, and the two formulations yield identical results.



**Figure 14:** Convergence of **u** for eccentric rotating cylinders under grid refinement. Our present two correction method is compared to the previous one correction method. Both methods converge under grid refinement, and the two correction algorithm is more accurate at coarser grid resolutions than the one correction method.

We compute v(x, y = 0) from x = -1 to x = 1 for both one and two correction methods, and compare their convergence properties in Figure 15. For cases in which  $\Delta s < h$ , the one correction formulation exhibits localized loss of accuracy near the subgrid interaction, whereas the two correction method maintains substantially improved accuracy. Even for the coarsest resolution with N = 16 grid cells in each direction, the two correction method captures the sharp velocity transition across the narrow gap.



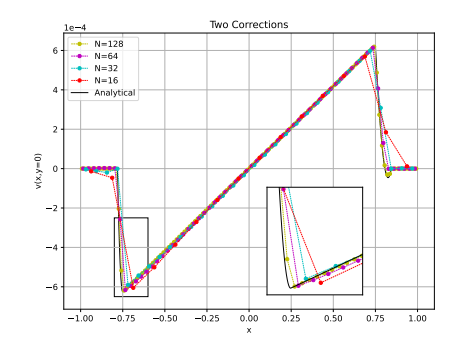


**Figure 15:** Convergence of the pointwise accuracy of the velocity profile v(x, y = 0) across eccentric rotating cylinders. Both methods converge under grid refinement, and the two correction algorithm is more accurate near the narrow gap at coarser resolutions than the one correction method.

Last, we analyze the accuracy of the two methods for various minimal separation distances between the cylinders in Figure 16. We fix the Cartesian grid resolution using N=64 grid cells in each direction. We set the center of the outer cylinder such that the minimal  $\Delta s$  is h,  $\frac{h}{2}$ ,  $\frac{h}{5}$ , and  $\frac{h}{10}$ , and compute v(x, y=0) across the narrow gap between the cylinders. As  $\Delta s \to 0$ , the one correction method exhibits a progressive loss of accuracy, whereas the two correction method reliably captures the pronounced velocity transition across the narrow interfacial gap for all tested separations.

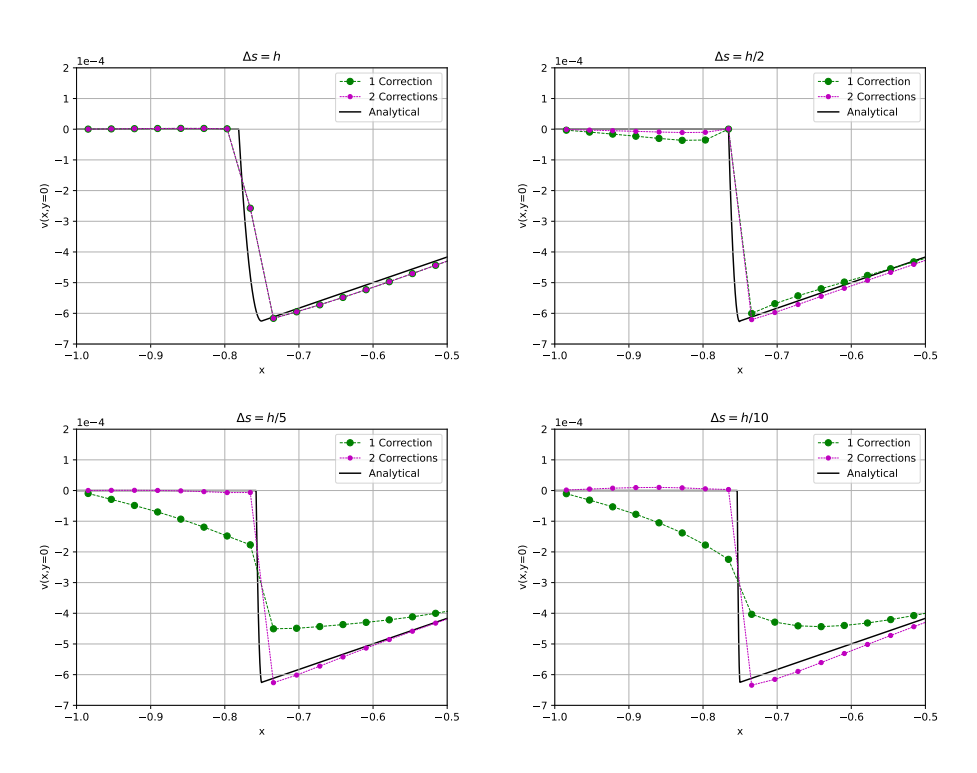


**Figure 16:** Comparison of the velocity profile v(x, y = 0) for various separations between two concentric rotating cylinders. When  $\Delta s < h$ , the two correction method shows greater accuracy than the one correction method.

#### 5 Discussion

This study demonstrates that our two correction IIM provides an effective approach to modeling flows between interfaces in near contact without requiring grid refinement. For both the concentric and eccentric rotating cylinder models, we observe substantial improvements in the accuracy of both Eulerian and Lagrangian velocity fields. In particular, the method maintains excellent accuracy for interface separations as small as  $\frac{h}{50}$ . Unlike lubrication-based approaches, <sup>18,19</sup> the present formulation does not rely on prior knowledge of interface orientation, separation distance, or analytic parameterizations, making it broadly compatible with finite element structural models and complex geometries. Our numerical experiments demonstrate notable improvements in velocity accuracy compared to a lubricated IB-based approach.

Future extensions of this work could include applications to elastic body FSI problems, as well as scenarios involving multiple interacting interfaces, which would naturally extend the framework to incorporate additional correction terms. Prohibitive computational cost remains the primary challenge in extending the two correction algorithm to three spatial dimensions. In particular, determining the intersection points between the second interface and the velocity interpolation stencil is computationally intensive, and this expense increases significantly as the interface resolution is refined.

# **Acknowledgments**

We gratefully acknowledge research support through NIH Awards R01HL157631, R03HL182166, and U01HL143336, and NSF award OAC 1931516. Computations were performed using facilities provided by University of North Carolina at Chapel Hill through the Research Computing division of UNC Information Technology Services. We gratefully acknowledge Dr. Ebrahim M. Kolahdouz for providing foundational code that facilitated the setup of our numerical experiments. We also thank Dr. David R. Wells for developing code infrastructure that facilitated the efficient implementation of our intersection algorithm.

This manuscript is the result of funding in whole or in part by the National Institutes of Health (NIH). It is subject to the NIH Public Access Policy. Through acceptance of this federal funding, NIH has been given a right to make this manuscript publicly available in PubMed Central upon the Official Date of Publication, as defined by NIH.

#### References

- <sup>1</sup> B. E. Griffith. Immersed boundary model of aortic heart valve dynamics with physiological driving and loading conditions. *International Journal for Numerical Methods in Biomedical Engineering*, 28(3):317–345, 2012.
- <sup>2</sup> C. S. Peskin. Flow patterns around heart valves: A numerical method. *Journal of Computational Physics*, 10(2):252–271, 1972.
- <sup>3</sup> Y. Zeng, Y. Wang, D. Yang, and Q. Chen. Immersed boundary methods for simulations of biological flows in swimming and flying bio-locomotion: A review. *Applied Sciences*, 13(7):4208, 2023.

- <sup>4</sup> E. M. Kolahdouz, D. R. Wells, S. Rossi, K. I. Aycock, B. A. Craven, and B. E. Griffith. A sharp interface Lagrangian-Eulerian method for flexible-body fluid-structure interaction. *Journal of Computational Physics*, 448:112174, 2023.
- <sup>5</sup> D. Xu, E. Kaliviotis, A. Munjiza, E. Avital, C. Ji, and J. Williams. Large scale simulation of red blood cell aggregation in shear flows. *Journal of Biomechanics*, 46(11):1810–1817, 2013.
- <sup>6</sup> D. Xu, C. Ji, E. Avital, E. Kaliviotis, A. Munjiza, and J. Williams. An investigation on the aggregation and rheodynamics of human red blood cells using high performance computations. *Scientifica*, 2017:1–10, 04 2017.
- <sup>7</sup> F. Liu, Z.M. Jin, F. Hirt, C. Rieker, P. Roberts, and P. Grigoris. Transient elastohydrodynamic lubrication analysis of metal-on-metal hip implant under simulated walking conditions. *Journal of Biomechanics*, 39(5):905–914, 2006.
- <sup>8</sup> A. Mayo. The fast solution of poisson's and the biharmonic equations on irregular regions. *SIAM Journal on Numerical Analysis*, 21(2):285–299, 1984.
- <sup>9</sup> R. J. LeVeque and Z. Li. The immersed interface method for elliptic equations with discontinuous coefficients and singular sources. *SIAM Journal on Numerical Analysis*, 31(4):1019–1044, 1994.
- <sup>10</sup> L. Lee and R. J. LeVeque. An immersed interface method for incompressible Navier–Stokes equations. *SIAM Journal on Scientific Computing*, 25(3):832–856, 2003.
- <sup>11</sup> Z. Li and M.-C. Lai. The immersed interface method for the Navier–Stokes equations with singular forces. *Journal of Computational Physics*, 171(2):822–842, 2001.
- $^{12}$  S. Xu and Z. J. Wang. Systematic derivation of jump conditions for the immersed interface method in three-dimensional flow simulation. *SIAM Journal on Scientific Computing*, 27:1948–1980, 2006.
- <sup>13</sup> N. Thekkethil and A. Sharma. Level set function–based immersed interface method and benchmark solutions for fluid flexible-structure interaction. *International Journal for Numerical Methods in Fluids*, 91(3):134–157, 2019.
- <sup>14</sup> J. Xu, W. Shi, W. Hu, and J. Huang. A level-set immersed interface method for simulating the electrohydrodynamics. *Journal of Computational Physics*, 400:108956, 2020.
- <sup>15</sup> E. M. Kolahdouz, A. P. Singh Bhalla, B. A. Craven, and B. E. Griffith. An immersed interface method for discrete surfaces. *Journal of Computational Physics*, 400:108854, 2020.
- <sup>16</sup> E. M. Kolahdouz, A. P. S. Bhalla, L. N. Scotten, B. A. Craven, and B. E. Griffith. A sharp interface Lagrangian-Eulerian method for rigid-body fluid-structure interaction. *Journal of Computational Physics*, 443:110442, 2021.
- <sup>17</sup> D. J. Acheson. *Elementary Fluid Dynamics*. Oxford University Press, 1990.
- <sup>18</sup> T. G. Fai and C. H. Rycroft. Lubricated immersed boundary method in two dimensions. *Journal of Computational Physics*, 356:319–339, 2018.

- <sup>19</sup> S. Xu, A. E. Yacoubi, and Z. J. Wang. A new method for computing particle collisions in Navier-Stokes flows. *Journal of Computational Physics*, 399:108919, 2019.
- <sup>20</sup> C. S. Peskin and B. F. Printz. Improved volume conservation in the computation of flows with immersed elastic boundaries. *Journal of Computational Physics*, 105(1):33–46, 1993.
- <sup>21</sup> B. E. Griffith and N. A. Patankar. Immersed methods for fluid–structure interaction. *Annual Review of Fluid Mechanics*, 52:421–448, 2020.
- <sup>22</sup> Z. Tan, D. Le, K. Lim, and B. Khoo. An immersed interface method for the incompressible navier–stokes equations with discontinuous viscosity across the interface. *SIAM Journal on Scientific Computing*, 31:1798–1819, 2009.
- <sup>23</sup> B. E. Griffith. On the volume conservation of the immersed boundary method. *Communications in Computational Physics*, 12(2):401–432, 2012.
- <sup>24</sup> B. E. Griffith. An accurate and efficient method for the incompressible Navier–Stokes equations using the projection method as a preconditioner. *Journal of Computational Physics*, 228(20):7565–7595, 2009.
- <sup>25</sup> W. J. Rider, J. A. Greenough, and J. R. Kamm. Accurate monotonicity- and extrema-preserving methods through adaptive nonlinear hybridizations. *Journal of Computational Physics*, 225(2):1827–1848, 2007.
- <sup>26</sup> P. Colella and P. R. Woodward. The Piecewise-Parabolic Method (PPM) for gas-dynamical simulations. *Journal of Computational Physics*, 54:174–201, 1984.
- <sup>27</sup> IBAMR: An Adaptive and Distributed-Memory Parallel Implementation of the Immersed Boundary Method. https://github.com/IBAMR/IBAMR.
- <sup>28</sup> SAMRAI: Structured Adaptive Mesh Refinement Application Infrastructure. http://www.llnl.gov/CASC/SAMRAI.
- <sup>29</sup> S. Balay, S. Abhyankar, M. F. Adams, S. Benson, J. Brown, P. Brune, K. Buschelman, E. M. Constantinescu, L. Dalcin, A. Dener, V. Eijkhout, J. Faibussowitsch, W. D. Gropp, V. Hapla, T. Isaac, P. Jolivet, D. Karpeev, D. Kaushik, M. G. Knepley, F. Kong, S. Kruger, D. A. May, L. C. McInnes, R. T. Mills, L. Mitchell, T. Munson, J. E. Roman, K. Rupp, P. Sanan, J. Sarich, B. F. Smith, S. Zampini, H. Zhang, H. Zhang, and J. Zhang. PETSc Web page. https://petsc.org/, 2025.
- <sup>30</sup> S. Balay, S. Abhyankar, M. F. Adams, S. Benson, J. Brown, P. Brune, K. Buschelman, E. Constantinescu, L. Dalcin, A. Dener, V. Eijkhout, J. Faibussowitsch, W. D. Gropp, V. Hapla, T. Isaac, P. Jolivet, D. Karpeev, D. Kaushik, M. G. Knepley, F. Kong, S. Kruger, D. A. May, L. C. McInnes, R. T. Mills, L. Mitchell, T. Munson, J. E. Roman, K. Rupp, P. Sanan, J. Sarich, B. F. Smith, H. Suh, S. Zampini, H. Zhang, H. Zhang, and J. Zhang. PETSc/TAO users manual. Technical Report ANL-21/39 Revision 3.24, Argonne National Laboratory, 2025.
- <sup>31</sup> S. Balay, W. D. Gropp, L. C. McInnes, and B. F. Smith. Efficient management of parallelism in object-oriented numerical software libraries. In E. Arge, A. M. Bruaset, and H. P. Langtangen, editors, *Modern Software Tools in Scientific Computing*, pages 163–202. Birkhauser Press, 1997.

<sup>&</sup>lt;sup>32</sup> hypre: High Performance Preconditioners. http://www.llnl.gov/CASC/hypre.

<sup>&</sup>lt;sup>33</sup> R. D. Falgout and U. M. Yang. *hypre*: A library of high performance preconditioners. In *International Conference on Computational Science*, pages 632–641. Springer, 2002.

<sup>&</sup>lt;sup>34</sup> libMesh: a C++ finite element library. http://libmesh.github.io.

<sup>&</sup>lt;sup>35</sup> B. S. Kirk, J. W. Peterson, R. H. Stogner, and G. F. Carey. libMesh: A C++ library for parallel adaptive mesh refinement/coarsening simulations. *Engineering Computations*, 22(3):237–254, 2006.